Check for updates

International Journal for Numerical Methods in Engineering

WILEY

RESEARCH ARTICLE OPEN ACCESS

Prediction of Cement Paste Elastic Properties via Computational Homogenization Using Digital Microstructures

Witold Ogierman[1,2] | Iwona Pokorska[2,3] | Tadeusz Burczyński[2]

[1]Faculty of Mechanical Engineering, Silesian University of Technology, Gliwice, Poland | [2]Institute of Fundamental Technological Research, Polish Academy of Sciences, Warsaw, Poland | [3]Faculty of Civil Engineering, Czestochowa University of Technology, Czestochowa, Poland

Correspondence: Witold Ogierman (witold.ogierman@polsl.pl)

Received: 11 June 2025 | **Revised:** 3 November 2025 | **Accepted:** 14 November 2025

Keywords: computational homogenization | micro-CT | micromechanics | multiscale modelling | representative volume element

ABSTRACT

This paper addresses the computational homogenization of cement paste, considering different types and sizes of representative volume elements (RVEs). Two microstructure models are examined: one generated from the simulation of hydration processes and the other based on microtomographic experimental data. A simplified three-phase virtual microstructure model is developed to enable a direct comparison between different model types. To generate this model, we have employed a multilevel analytical Mori–Tanaka approach to the preliminary homogenization of anhydrous cement grains and hydration products. Computational homogenization is performed using a fast Fourier transform (FFT)-based method. A very good agreement is observed between the results of the proposed simplified model and those of the original model. Moreover, local stress distributions at the microstructural level are analyzed. Our findings provide new insights into how cement paste's effective elastic properties vary with different volume element sizes and microstructure model types. We demonstrate that the required size of RVEs depends on the microstructure model type and highlight potential differences between results obtained for different RVE sizes. For relatively large RVE sizes, good agreement is observed between the results obtained from the simulated and experimentally based microstructure models. We also investigated the symmetry type of the determined effective elastic tensors. These findings may facilitate the multiscale modelling of cement paste and lead to a better understanding of the relationship between microstructural features and effective elastic behavior.

1 | Introduction

Cement paste is a binder for cementitious materials, playing a crucial role in developing construction materials. The microstructure of cement paste, formed during the hydration process, typically comprises a combination of various hydration products, unreacted clinker particles and pores. Developing microstructure-informed micromechanical modelling

This is an open access article under the terms of the Creative Commons Attribution-NonCommercial-NoDerivs License, which permits use and distribution in any medium, provided the original work is properly cited, the use is non-commercial and no modifications or adaptations are made.
© 2025 The Author(s). *International Journal for Numerical Methods in Engineering* published by John Wiley & Sons Ltd.

of cement paste is becoming increasingly popular since it provides a relationship between microstructural features and effective behavior at the macroscale, potentially enhancing the understanding of cement paste's behavior. The reader is kindly referred to the review paper by Zhang et al. [1], who have provided an overview of aspects associated with the micromechanical modelling of cement paste. Although experimental and numerical techniques have been proposed in the literature to generate models of the microstructure of cement paste, microstructure-informed modelling remains challenging due to the complex, multicomponent nature of this microstructure. The subsequent paragraphs of this introduction address the following topics: (i) microstructure reconstruction based on X-ray microtomography, (ii) generation of microstructure models via computer simulations of the hydration process, (iii) generation of statistically equivalent microstructure models, (iv) approaches for modelling different material phases, and (v) the aim and scope of this study.

Following the experimental approach, three-dimensional models of microstructures can be generated based on the results of X-ray microtomography. One of the pioneering works in reconstructing the microstructure of cement paste with a resolution of less than 1 μmwas conducted by Bentz et al. [2] and Gallucci et al. [3]. Although X-ray microtomography allows obtaining a three-dimensional microstructure model, typically, it is difficult to segment all hydration products since they have similar X-ray attenuation coefficients [4]. Therefore, the microstructure is often represented as a three-component composite consisting of homogenized hydration products, anhydrous clinker, and pores [5–8]. Gallucci et al. [3] additionally reconstructed the portlandite phase (CH). On the other hand, Kim et al. [9], focusing on the pore distribution, idealized the cement phase as a two-phase material comprising pores and solid phase. The numerical model of cement paste based on the microtomographic data was developed by Hain and Wriggers [10], who applied a finite element (FE)-based homogenization procedure. The authors demonstrated that a three-dimensional representative volume element (RVE) consisting of 72^3 FEs (size of each cubic element is $1 \times 1 \times 1$ μm) is not large enough to capture the effective properties of cement paste with sufficient accuracy. Consequently, they adopted a statistical approach, analyzing many different RVEs consisting of 64^3 elements in order to capture effective properties accurately. Another FE-based study of effective elastic properties of cement paste utilizing microtomographic data was conducted by Huang et al. [7]. Zhang et al. [11–13] also developed numerical models of cement paste microstructure based on the microtomographic data. However, they used the lattice model which treats material as a grid of beam elements. Different types of lattice elements have been defined in order to capture interactions between different phases. Zhang and Jivkov [6, 8] proposed a different lattice model based on truncated-octahedral cells known as the site-bond model which also incorporates microtomographic data. Zhang et al. [14] reported an approach which does not require explicit identification of distinct phases; the intrinsic heterogeneity of cement paste is directly treated using greyscale images obtained by μCT and using a linear relationship between Young's modulus and greyscale level.

Another method for generating a model of the cement paste's microstructure is conducting computer simulations of the hydration process. The most popular software packages allowing the generation of the microstructure as the result of the hydration process are CEMHYD3D [15, 16], HYMOSTRUCT3D [17], and μic [18]. Another well-known software for modelling the cement paste's microstructure is Virtual Cement and Concrete Testing Laboratory (VCCTL), which uses the CEMHYD3D as the hydration model [19]. The VCCTL software furthermore allows determining the elastic moduli of cement materials by incorporating implemented finite element method (FEM) based homogenization [20]. Moreover, the hydration of cement paste can be simulated thermodynamically using the GEM-Selektor software [21, 22]. Using microstructure models derived by hydration process simulation, Haecker et al. [23] computed the effective elastic properties of cement paste by analysing three-dimensional RVEs with the FEM. According to the authors, a $100 \times 100 \times 100$ μm RVE is typical for elastic properties predictions, while early-age cement paste necessitates increased resolution. Mazaheripour et al. [24] also incorporated hydration-simulation–derived microstructures into an FE-based analysis. They further compared the elastic properties obtained from the FE model with those from the previously mentioned lattice model, finding reasonable agreement. Rhardane et al. [25] performed hydration simulations to generate an RVE of $200 \times 200 \times 200$ μm; however, they subsequently employed simplified two-dimensional FE models by extracting 2D sections from the 3D volume. This simplification was justified, as full 3D FE computations were computationally prohibitive due to the high voxel count. Šmilauer and Bažant [26] also used the outcome of hydration simulation to prepare the model of the microstructure; however they used the fast Fourier transform (FFT)-based homogenization. In this case, an RVE of size $50 \times 50 \times 50$ μm was utilized. In recent years, the FFT-based homogenization, which originates from the pioneering works of Moulinec and Suquet [27, 28], has become popular in modelling composite materials [29–35].

Another different approach in preparing models of cement paste microstructure is based on generation of statistically equivalent geometries. Thilakarathna et al. [36] utilized simplified microstructure models by treating the clinker phases, CH, and voids as spherical inhomogeneities randomly distributed in the RVE's volume, with volume fractions derived from hydration process simulations using VCCTL software. A method for generating RVEs by randomly placing

10970207, 2025, 24, Downloaded from https://onlinelibrary.wiley.com/doi/10.1002/nme.70200 by Instytut Podstawowych Problemow Techniki PAN, Wiley Online Library on [11/12/2025]. See the Terms and Conditions (https://onlinelibrary.wiley.com/terms-and-conditions) on Wiley Online Library for rules of use; OA articles are governed by the applicable Creative Commons License

nonoverlapping particles of different shapes, corresponding to the main constituents of cement paste, has also been presented by Bary et al. [37]. It is also worth mentioning that, besides the computational homogenization, mean field homogenization methods such as Mori–Tanaka or self-consistent methods are frequently applied [38–42].

It should be also underlined that the literature presents various approaches to addressing the multicomponent nature of the cement paste microstructure to generate models for predicting effective elastic properties. One of the main differences between the models is the treatment of the calcium silicate hydrate (C-S-H) phase; one of the models involves inner and outer products of hydration (low-density C-S-H and high-density C-S-H) [11–13, 24, 26], and another way is to involve a single homogenous C-S-H phase (whose properties can be for example determined by homogenizing low-density and high-density C-S-H phases on the lower scale) [6, 23, 25, 36, 39, 42, 43]. Further differences can be observed in the treatment of the portlandite phase (CH). Some studies include this phase in their models [14, 16, 20, 22–24], while others omit it for simplification [6, 15, 17–19, 21, 25]. The anhydrous clinker phases, such as alite, and so on, are often treated as single phases due to relatively low differences in their stiffness [6, 14–22]. On the other hand, some works consider different properties of the clinker phases [25, 26, 44]. The common feature of the models from the literature is the consideration of pores in the microstructure models. Although the geometrical representation of other hydration products, such as ettringite and hydrogarnet, can be obtained by using, for instance, VCCTL software, their elastic properties are most often taken as the same as the C-S-H matrix or CH [23]. On the other hand, Rhardane et al. [25] used a simplified two-dimensional model of the microstructure with prescribed individual elastic properties for the mentioned phases.

A detailed microtomographic investigation of cement paste, including an analysis of the size of anhydrous clinker grains, was conducted by Hlobil et al. [5]. The authors of that study postulated that a RVE for cement paste should be approximately 150–200 μm (length of a cube's edge) to represent cement grains accurately. This RVE size was proposed based on common design requirements, which suggest that the RVE should be 5–10 times the characteristic heterogeneity size [5]; however, direct computational homogenization has not been conducted. Therefore, our paper aims to verify this recommendation by performing numerical homogenization using both virtually generated microstructures and microtomographic data provided by Hlobil et al. [45]. Such verification is also warranted given the variability in RVE sizes reported for cement-paste microstructures in the literature. We generated the virtual microstructure using VCCTL software, with an initial model size of $300 \times 300 \times 300$ μm. We then progressively reduced its dimensions to investigate the influence of RVE size on the effective elastic properties. Additionally, we emphasize the investigation of local stiffness variations throughout the cement paste volume. We also investigated the symmetry type of the determined effective elastic tensor and its deviation from perfect isotropy concerning the RVE size. During this study, we have applied FFT-based homogenization due to excellent time efficiency compared to FEM [46]. Employing the FFT-based homogenization substantially mitigated the prohibitive computation times encountered with FE-based approaches for large RVEs. Besides homogenization, we have examined the distribution of stresses at the microstructural level, both for the virtually generated microstructure and for that obtained using microtomographic data. We aim to verify whether the local stress distributions obtained from different microstructure models are consistent. This is an important issue, as such models reveal the stresses in different phases and may also be used to predict failure initiation and progression at the microscale (e.g., Hain and Wriggers [10], Rhardane et al. [25]). We have visualized the principal stress distributions for the RVEs and, additionally, presented the probability density functions of the principal stress in the unreacted clinker phase. The comparison aims to verify if the hydration simulation-based microstructure models yield comparable results to experimentally obtained models. A table listing the symbols used throughout the paper is provided in Appendix A.

2 | Materials and Methods

2.1 | Virtual Model of the Microstructure and Homogenization

The virtual model of the microstructure was generated based on the output of a computer simulation of the hydration process, conducted using the VCCTL software. The volume contents of the main cement minerals considered were as follows: $\phi C_3S = 0.7815$, $\phi C_2S = 0.0477$, $\phi C_3A = 0.0604$, and $\phi C_4AF = 0.1103$. The water-to-cement ratio was set up as 0.35, and the state after 28 days of hydration was assumed. These values were selected to align with the specifications of the available microtomographic data [45] and enable further comparison of the results. The volume representing the microstructure of cement paste, as shown in Figure 1, consists of 300^3 voxels, each with a size of $1 \times 1 \times 1$ μm (the length of a cube's edge is 300 μm). Table 1 presents the phases and their volume fractions obtained from the hydration process simulation. Moreover, the elastic constants related to these phases have been included. It should be emphasized that the procedure of initial spatial configuration of cement particles prior to conducting hydration simulation has a random nature. Consequently, the

10970207, 2025, 24, Downloaded from https://onlinelibrary.wiley.com/doi/10.1002/nme.70200 by Instytut Podstawowych Problemow Techniki PAN, Wiley Online Library on [11/12/2025]. See the Terms and Conditions (https://onlinelibrary.wiley.com/terms-and-conditions) on Wiley Online Library for rules of use; OA articles are governed by the applicable Creative Commons License

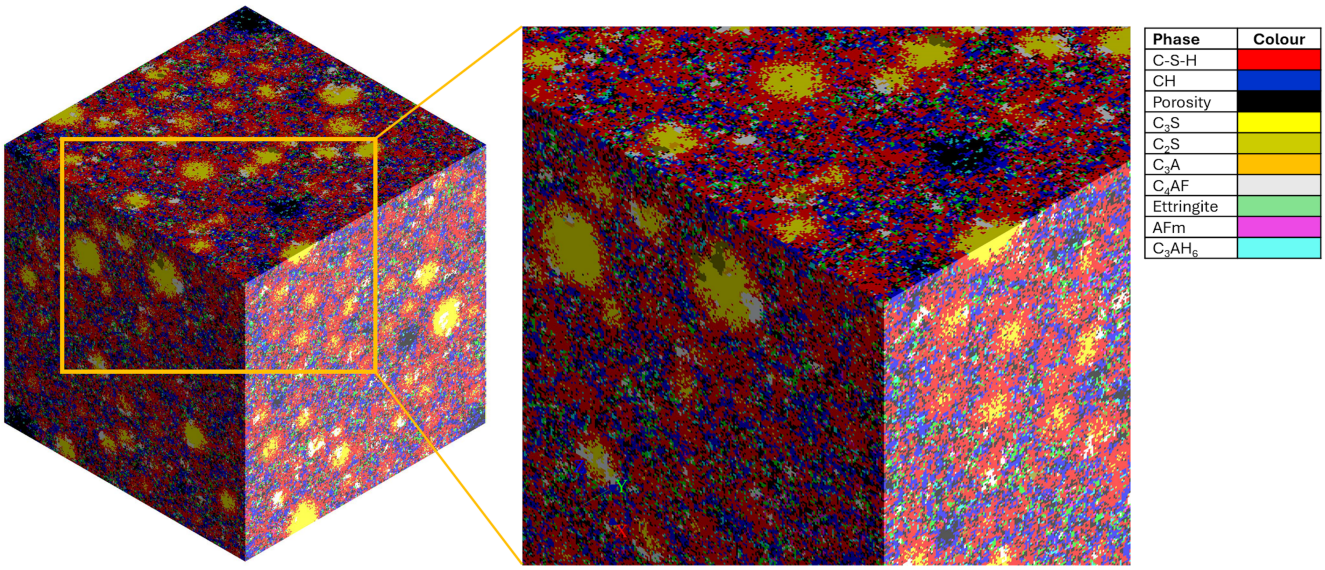

FIGURE 1 | Virtual model of the cement paste microstructure generated as the outcome of the hydration simulation.

TABLE 1 | Constituents of the cement paste: Volume fractions obtained from the hydration process simulation and elastic constants related to the phases.

Phase	Volume fraction	Young modulus, MPa	Poisson ratio	References
C-S-H (calcium silicate hydrate)	0.4392	23,800	0.24	[47]
CH (portlandite)	0.1750	38,000	0.31	[47]
Porosity	0.1678	—	—	
C_3S (alite)	0.0709	135,000	0.30	[48]
C_2S (belite)	0.0081	130,000	0.30	[48]
C_3A (cubic tricalcium aluminate)	0.0046	145,000	0.30	[48]
C_4AF (tetracalcium aluminoferrite)	0.0261	125,000	0.30	[48]
Ettringite	0.0563	29,670	0.34	[49]
AFm (generic monosulfate)	0.0186	32,140	0.36	[49]
C_3AH_6 (hydrogarnet)	0.0333	54,900	0.22	[49]

outcomes of hydration process simulations performed with VCCTL software, which rely on random particle placement, are nondeterministic. As a result, the spatial distribution of phases may differ between simulation runs, and the corresponding phase volume fractions can exhibit slight variations. Nonetheless, the differences between outcomes from different simulation runs are not substantial. To illustrate the extent of these discrepancies, the results of an additional hydration process simulation are provided in Appendix B, where both the obtained geometrical model and the phase volume fractions are presented.

Afterward, the voxel-based model of the microstructure was transferred to Digimat software [50], where the integrated FFT-based solver was utilized to perform the solution of the following boundary value problem:

$$\begin{cases} \operatorname{div}(\boldsymbol{\sigma}) = 0, \quad \forall \mathbf{x} \in \Omega & \text{(equilibrium)} \\ \boldsymbol{\varepsilon}(\mathbf{x}) = \frac{1}{2}\left(\nabla \mathbf{u}(\mathbf{x}) + \nabla^{\mathrm{T}} \mathbf{u}(\mathbf{x})\right), \forall \mathbf{x} \in \Omega & \text{(kinematics)} \\ \boldsymbol{\sigma}(\mathbf{x}) = \mathbf{C}_{\mathrm{p}}(\mathbf{x}) : \boldsymbol{\varepsilon}(\mathbf{x}), \forall \mathbf{x} \in \Omega & \text{(constitutive model)} \\ \mathbf{u}(\mathbf{x}) \text{ is periodic}, \forall \mathbf{x} \in \partial\Omega & \text{(periodic boundary conditions)} \\ \langle \boldsymbol{\varepsilon} \rangle = \mathbf{E} & \text{(imposed mean value)} \end{cases}, \tag{1}$$

10970207, 2025, 24, Downloaded from https://onlinelibrary.wiley.com/doi/10.1002/nme.70200 by Instytut Podstawowych Problemow Techniki PAN, Wiley Online Library on [11/12/2025]. See the Terms and Conditions (https://onlinelibrary.wiley.com/terms-and-conditions) on Wiley Online Library for rules of use; OA articles are governed by the applicable Creative Commons License

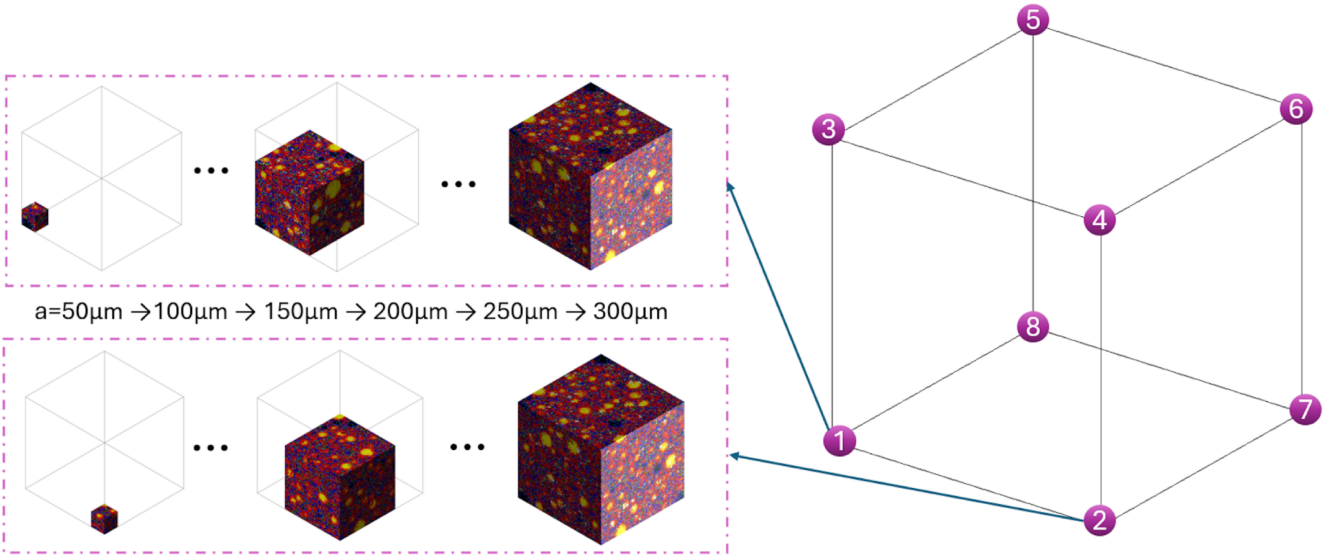

FIGURE 2 | Scheme illustrating the investigation of the influence of the representative volume element (RVE) size on its effective properties and local variation of stiffness.

where $\boldsymbol{\sigma}$ denotes the Cauchy stress tensor, $\boldsymbol{\varepsilon}$ represents the infinitesimal strain tensor, and $\mathbf{u}$ is the displacement vector. Ω denotes the domain of the RVE, while $\partial\Omega$ represents its boundary where periodic boundary conditions have been imposed ($\mathbf{E}$ is assumed as the prescribed macroscopic strain tensor). The elastic stiffness tensor $\mathbf{C}_p$ can vary between grid points and is associated with the elastic constants of the phases listed in Table 1. We assume an isotropic behavior for individual phases. Therefore, the elastic stiffness tensor for each grid point can be defined using the Young's modulus and Poisson's ratio. The effective stiffness tensor $\mathbf{C}$ representing behavior of the cement paste can be determined by computing the macroscopic stress resulting from the six elementary macroscopic strain states [51]. In this paper, we investigate the influence of the RVE size on its effective properties while also examining the local variations of these properties. To achieve this, we conducted several numerical experiments related to the computational homogenization, utilizing various sizes and positions of cubic volumes. The volume was gradually increased, starting from an element size of $50 \times 50 \times 50$ μm ($a = 50$ μm) located at one of the vertices of a larger cubic domain of size $300 \times 300 \times 300$ μm ($a = 300$ μm). This procedure is illustrated schematically in Figure 2. The mentioned analyses were performed starting from all eight vertices marked in Figure 2, including the computation of the effective elastic stiffness tensors for each case. A limitation of such analysis, which should be mentioned, is that subcubes extracted from a single larger RVE are not statistically independent when a exceeds 150 μm.

Moreover, we have investigated a relationship between the RVE size and symmetry of the effective elastic stiffness tensor. For that reason, the following parameter has been proposed:

$$s_r = R_{11} + R_{12} + R_{13} + R_{22} + R_{23} + R_{33} + R_{44} + R_{55} + R_{66}, \tag{2}$$

where R is the following matrix:

$$R_{ij} = \begin{bmatrix} \frac{|\tilde{C}_{11}-C_{11}|}{\tilde{C}_{11}} & \frac{|\tilde{C}_{12}-C_{12}|}{\tilde{C}_{12}} & \frac{|\tilde{C}_{13}-C_{13}|}{\tilde{C}_{13}} & & & & \\ & \frac{|\tilde{C}_{22}-C_{22}|}{\tilde{C}_{22}} & \frac{|\tilde{C}_{23}-C_{23}|}{\tilde{C}_{23}} & & & & \\ & & \frac{|\tilde{C}_{33}-C_{22}|}{\tilde{C}_{33}} & & & & \\ & & & \frac{|\tilde{C}_{44}-C_{44}|}{\tilde{C}_{44}} & & & \\ & & & & \frac{|\tilde{C}_{55}-C_{55}|}{\tilde{C}_{55}} & & \\ & & & & & \frac{|\tilde{C}_{66}-C_{66}|}{\tilde{C}_{66}} & \end{bmatrix}, \tag{3}$$

where:

$$\tilde{C}_{11} = \tilde{C}_{22} = \tilde{C}_{33} = \frac{C_{11} + C_{22} + C_{33}}{3}, \tilde{C}_{12} = \tilde{C}_{13} = \tilde{C}_{23} = \frac{C_{12} + C_{13} + C_{23}}{3}, \tilde{C}_{44} = \tilde{C}_{55} = \tilde{C}_{66} = \frac{C_{44} + C_{55} + C_{66}}{3}. \tag{4}$$

10970207, 2025, 24, Downloaded from https://onlinelibrary.wiley.com/doi/10.1002/nme.70200 by Instytut Podstawowych Problemow Techniki PAN, Wiley Online Library on [11/12/2025]. See the Terms and Conditions (https://onlinelibrary.wiley.com/terms-and-conditions) on Wiley Online Library for rules of use; OA articles are governed by the applicable Creative Commons License

Furthermore we considered for analysis another parameter:

$$t_r = Z_{11} + Z_{12} + Z_{13} + Z_{22} + Z_{23} + Z_{33} + Z_{44} + Z_{55} + Z_{66}, \tag{5}$$

where Z is the following matrix:

$$Z_{ij} = \begin{bmatrix} \frac{|C_{11}^{ISO} - C_{11}|}{C_{11}^{ISO}} & \frac{|C_{12}^{ISO} - C_{12}|}{C_{12}^{ISO}} & \frac{|C_{13}^{ISO} - C_{13}|}{C_{13}^{ISO}} & & & \\ & \frac{|C_{22}^{ISO} - C_{22}|}{C_{22}^{ISO}} & \frac{|C_{23}^{ISO} - C_{23}|}{C_{23}^{ISO}} & & & \\ & & \frac{|C_{33}^{ISO} - C_{22}|}{C_{33}^{ISO}} & & & \\ & & & \frac{|C_{44}^{ISO} - C_{44}|}{C_{44}^{ISO}} & & \\ & & & & \frac{|C_{55}^{ISO} - C_{55}|}{C_{55}^{ISO}} & \\ & & & & & \frac{|C_{66}^{ISO} - C_{66}|}{C_{66}^{ISO}} \end{bmatrix}, \tag{6}$$

where:

$$C^{ISO} = \begin{bmatrix} \lambda + 2\mu & \lambda & \lambda & 0 & 0 & 0 \\ \lambda & \lambda + 2\mu & \lambda & 0 & 0 & 0 \\ \lambda & \lambda & \lambda + 2\mu & 0 & 0 & 0 \\ 0 & 0 & 0 & \mu & 0 & 0 \\ 0 & 0 & 0 & 0 & \mu & 0 \\ 0 & 0 & 0 & 0 & 0 & \mu \end{bmatrix} \tag{7}$$

is stiffness matrix defined by Lame constats, which stand for the best isotropic approximation of an anisotropic stiffness tensor provided by Cavallini [52]:

$$\lambda = \frac{1}{15}\left[C_{11} + C_{22} + C_{33} - 2\left(C_{44} + C_{55} + C_{66}\right) + 4\left(C_{12} + C_{13} + C_{23}\right)\right] \tag{8}$$

$$\mu = \frac{1}{15}\left[C_{11} + C_{22} + C_{33} + 3\left(C_{44} + C_{55} + C_{66}\right) - \left(C_{12} + C_{13} + C_{23}\right)\right]. \tag{9}$$

The approximation proposed by Cavallini is based on the orthogonal projection of the anisotropic elasticity tensor into the isotropic subspace. Furthermore, to assess if the material symmetry is isotropy or cubic we have determined a Zener ratio for each analyzed case [53]:

$$a_r = \frac{2\tilde{C}_{44}}{\tilde{C}_{11} - \tilde{C}_{12}}. \tag{10}$$

Although the Zener ratio was originally proposed to quantify anisotropy in cubic crystals, it can also be used to assess the anisotropy of engineering materials [54, 55]. For a perfectly isotropic material, the Zener ratio equals 1. Deviations from 1 indicate the degree of elastic anisotropy (considered cubic in this context).

2.2 | Mori–Tanaka Method and Simplified Virtual Model of the Microstructure

The Mori–Tanaka method is one of the most frequently used mean-field homogenization methods. It has been applied to model cement paste in numerous studies. In our work, we used the Mori–Tanaka method for two reasons. The first is to obtain a reference solution for the results obtained through numerical analysis. The second is to generate a simplified virtual model of the microstructure. To address the multiphase nature of cement paste, we have employed a multilevel Mori–Tanaka approach [56], as the original formulation of this method is designed for two-phase composites. Thus, at each level of homogenization a well-known expression for the effective elastic stiffness tensor of two-phase composite $\mathbf{C}_{MT}$ has been applied [57]:

$$\mathbf{C}_{MT} = \mathbf{C}_m + f_i\left(\mathbf{C}_i - \mathbf{C}_m\right)\mathbf{A}\left[f_m\mathbf{I} + f_i\mathbf{A}\right]^{-1}, \tag{11}$$

10970207, 2025, 24, Downloaded from https://onlinelibrary.wiley.com/doi/10.1002/nme.70200 by Instytut Podstawowych Problemow Techniki PAN, Wiley Online Library on [11/12/2025]. See the Terms and Conditions (https://onlinelibrary.wiley.com/terms-and-conditions) on Wiley Online Library for rules of use; OA articles are governed by the applicable Creative Commons License

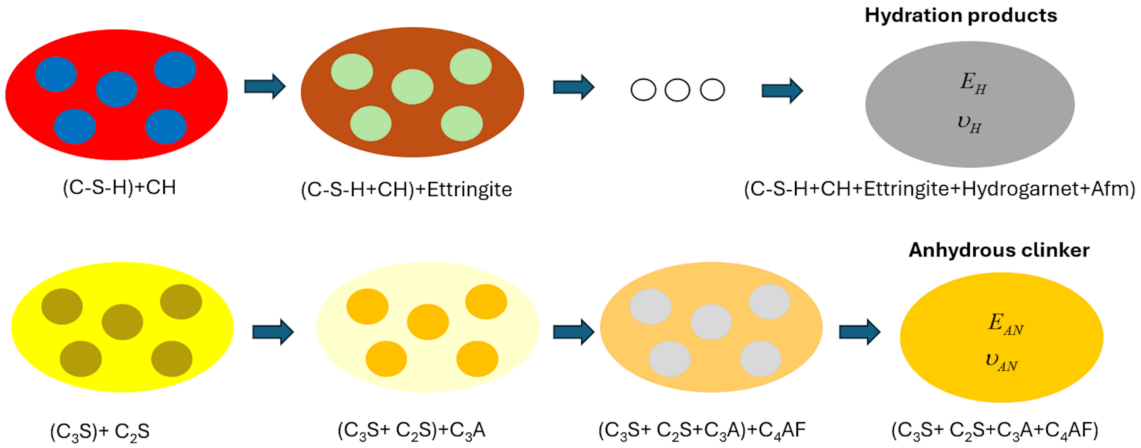

FIGURE 3 | Scheme of the first stage of the multilevel homogenization.

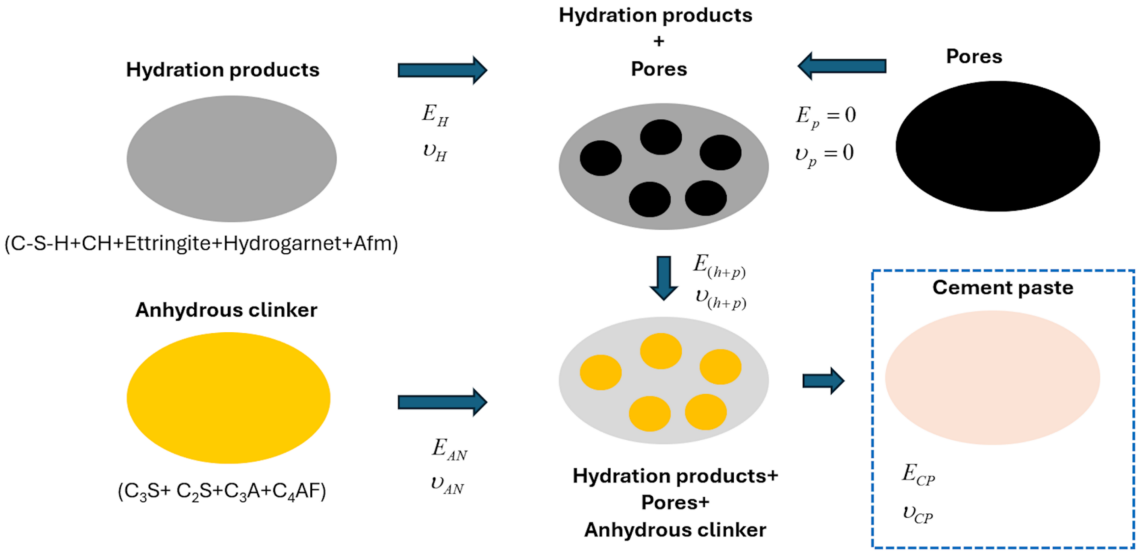

FIGURE 4 | Scheme of the second stage of the multilevel homogenization.

where **A** is the strain concentration tensor defined as:

$$\mathbf{A} = \left[\mathbf{I} + \mathbf{S}\mathbf{C}_m^{-1}\left(\mathbf{C}_i - \mathbf{C}_m\right)\right]^{-1}, \tag{12}$$

where $\mathbf{C}_m$ and $\mathbf{C}_i$ are the stiffness tensors for matrix and inhomogeneity respectively, f_m and f_i are the volume fractions of matrix and inhomogeneities, **I** is the identity tensor, and **S** is Eshelby's tensor. In this case, we have used the Eshelby's tensor for spherical inclusion, presented for instance in work of Mura [58]. The homogenization process is conducted in two distinct stages. In the first stage, we perform multilevel homogenization to determine the properties of both the hydration products and the anhydrous clinker (see Figure 3). In the second stage, we apply a two-level homogenization approach: first, we homogenize the hydration products with the pores, and then we incorporate the anhydrous particles at the second level (see Figure 4). Finally, the effective elastic properties of cement paste are obtained. Moreover, the properties of hydration products and anhydrous clinker, which are products of the first stage of homogenization, are used to create a simplified three-phase virtual model of the microstructure. The procedure of generation of the mentioned model is schematically presented in Figure 5. Here, the voxels in which the properties of clinker phases (C_3S, C_2S, C_3A, C_4AF) are prescribed are unified, and the properties of homogenized anhydrous clinker (E_{AN}, ν_{AN}) are assigned instead. A similar operation is performed for voxels representing hydration products (C-S-H, CH, ettringite, hydrogarnet, and AFm), which are unified and assigned homogenized elastic properties (E_H, ν_H). Generation of such a three-phase model is necessary to make a direct comparison with the results obtained through the model based on a microtomographic data, which is described in Section 2.3.

10970207, 2025, 24, Downloaded from https://onlinelibrary.wiley.com/doi/10.1002/nme.70200 by Instytut Podstawowych Problemow Techniki PAN, Wiley Online Library on [11/12/2025]. See the Terms and Conditions (https://onlinelibrary.wiley.com/terms-and-conditions) on Wiley Online Library for rules of use; OA articles are governed by the applicable Creative Commons License

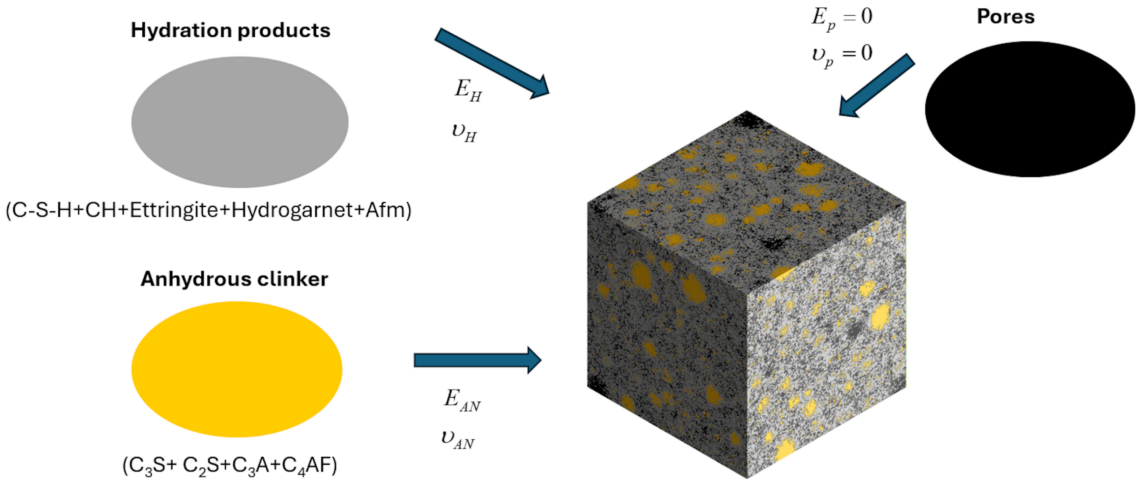

FIGURE 5 | A simplified three-phase virtual model of the microstructure.

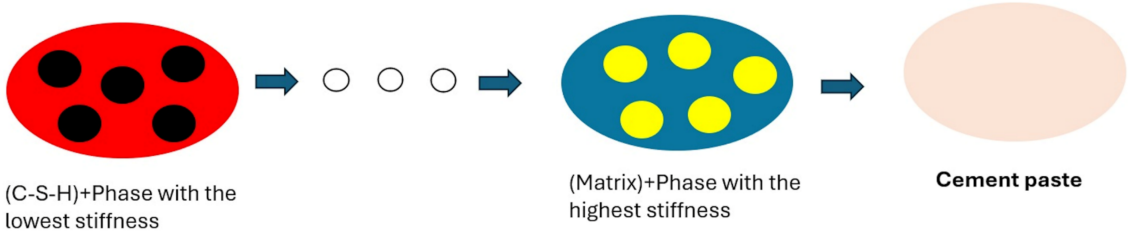

FIGURE 6 | Scheme of the sequential multilevel homogenization (without dividing into two stages).

Moreover, for comparison, we conducted the Mori–Tanaka multilevel homogenization sequentially, starting by adding the phase with the lowest stiffness to the C-S-H matrix and incorporating other phases in ascending order of stiffness (Figure 6). The recommendation to add the inclusions from the most compliant to the most rigid can be found in [59]. Moreover, Doghri et al. [56] analyzed fiber-reinforced composites with voids and showed that the best accuracy is obtained when, at the first level, voids are homogenized with the matrix, and then the fibers are homogenized with the new matrix obtained in the first step.

2.3 | Model of the Microstructure Based on the Microtomographic Data

We used the data published by Hlobil et al. [45] to generate the numerical model based on the microstructure of real material. The mentioned data covers different cases of hydration times; in this study, we have considered the case of a water-to-cement ratio of 0.35 and a hydration time of 28 days. Since the provided data involves the volumes of cubes of approximate edge length 500 μm, we have consistently reduced the size of the region of interest to the size of the previously discussed virtual microstructure model (300 μm). The data in the form of a grayscale map was segmented using the Otsu method [4, 60, 61], extended to extracting pores as well as the anhydrous clinker grains. For that purpose, we utilized the "Volume Segmenter" MATLAB toolbox. The obtained model of the microstructure is visualized in Figure 7. It must be mentioned that there is a slight difference in voxel size between the models presented in Figures 1 and 7. In the first case, the capabilities of the VCCTL software dictate the voxel size of 1 μm. In contrast, the microtomographic data corresponds to a voxel size of approximately 1.1 μm in the second case.

3 | Results and Discussion

3.1 | Results of the Homogenization

Before performing the planned numerical analyses, the influence of the density of the Fourier point grid on the effective properties was examined. Although a regular grid of Fourier points can be directly used from the voxel representation of

10970207, 2025, 24, Downloaded from https://onlinelibrary.wiley.com/doi/10.1002/nme.70200 by Instytut Podstawowych Problemow Techniki PAN, Wiley Online Library on [11/12/2025]. See the Terms and Conditions (https://onlinelibrary.wiley.com/terms-and-conditions) on Wiley Online Library for rules of use; OA articles are governed by the applicable Creative Commons License

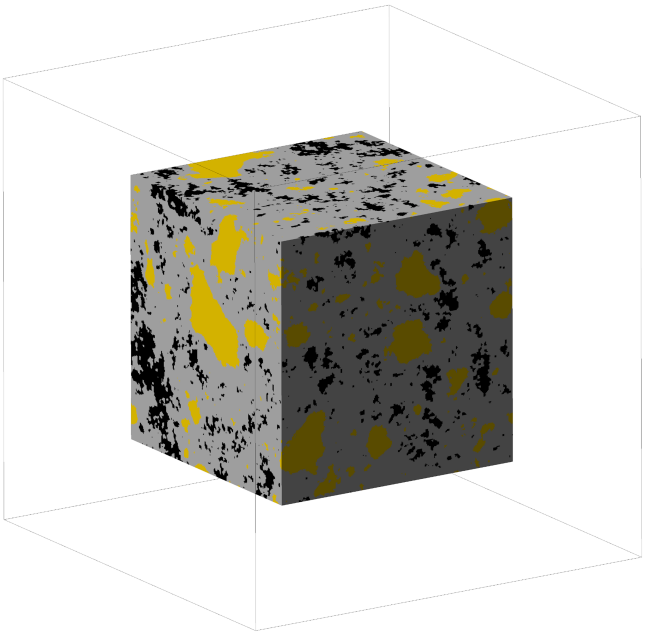

FIGURE 7 | Model of the cement paste microstructure generated based on the microtomographic experimental data.

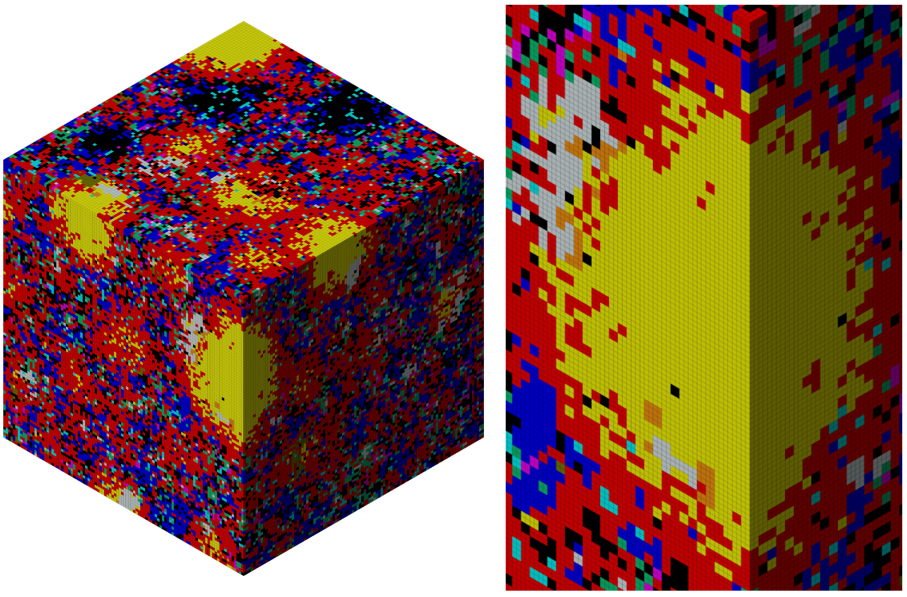

a) b)

FIGURE 8 | Grid of Fourier points: (a) based directly of voxel representation of the microstructure model (distance between points 1 μm), (b) each voxel is divided into eight voxels (distance between points 0.50 μm)—a detailed view.

the microstructure model without the need for meshing, these voxels can be further subdivided to provide a denser grid. To test the effect of grid size on the results, a case of an RVE with a size of $100 \times 100 \times 100$ μm, extracted from the center of the model presented in Figure 1, was considered. Three grid sizes have been accounted for: 1, 0.5, and 0.25 μm (sizes 1, and 0.5 μm have been visualized in Figure 8). Table 2 contains the obtained effective elastic constants. The presented values are the averages of Young's modulus, Poisson's ratio, and shear modulus, calculated from the values collected for different directions based on the effective elastic stiffness tensor. The advantage of using a grid size of 0.50 μm instead of 1 μm is clearly noticeable for Young's modulus, where there is an almost 7% relative difference between the results. Further increasing the grid density to 0.25 μm could improve accuracy. However, the differences between the results obtained for grid sizes of 0.25 and 0.50 μm do not exceed 2%. Therefore, in all further computations, we used a grid size of 0.50 μm to

10970207, 2025, 24, Downloaded from https://onlinelibrary.wiley.com/doi/10.1002/nme.70200 by Instytut Podstawowych Problemow Techniki PAN, Wiley Online Library on [11/12/2025]. See the Terms and Conditions (https://onlinelibrary.wiley.com/terms-and-conditions) on Wiley Online Library for rules of use; OA articles are governed by the applicable Creative Commons License

TABLE 2 | Influence of grid size on the effective properties, quantities are averaged values from ones obtained for different loading directions.

	Grid size (distance between nearest Fourier points)		
Effective property	**1.00 μm**	**0.50 μm**	**0.25 μm**
Young modulus—E	20.788 GPa	19.481GPa	19.411GPa
Poisson ratio—ν	0.2339	0.2313	0.2278
Shear modulus—G	7.549 GPa	7.547 GPa	7.419 GPa

TABLE 3 | Effective properties of phases obtained using the Mori–Tanaka method for application in a 3-phase model.

Effective property	Hydration products	Anhydrous clinker
Young modulus—E	28.364 GPa	132.580 GPa
Poisson ratio—ν	0.2673	0.3000

establish a balance between accuracy and computational time (e.g., for an RVE size of 300 μm, using a grid size of 0.50 μm results in 216 million points, while a grid size of 0.25 μm leads to 1.728 billion points).

The effective stiffness tensor determined for the case of the RVE of size 300 μm visualized in Figure 1 has the following form:

$$C_{VCCTL} = \begin{bmatrix} 24.028 & 7.310 & 7.304 & 0.011 & 0.005 & -0.013 \\ 7.310 & 24.073 & 7.320 & -0.011 & 0.032 & -0.010 \\ 7.304 & 7.320 & 24.101 & 0.003 & 0.018 & 0.017 \\ 0.011 & -0.011 & 0.003 & 8.023 & -0.009 & 0.009 \\ 0.005 & 0.032 & 0.018 & -0.009 & 8.039 & 0.003 \\ -0.013 & -0.010 & 0.017 & 0.009 & 0.003 & 8.021 \end{bmatrix}, \text{GPa} \tag{13}$$

Using the approach illustrated in Figure 5, the effective properties of hydration products and anhydrous clinker were determined using the Mori–Tanaka homogenization method prior to obtaining the results for the model based on the microtomographic data. The values obtained are collected in Table 3.

Below is the effective stiffness tensor obtained for the model generated using the VCCTL software with dimensions of 300 μm, considering a three-phase representation and incorporating the elastic constants from Table 3:

$$C_{VCCTL\_3PHASE} = \begin{bmatrix} 23.926 & 7.295 & 7.290 & 0.012 & 0.008 & -0.016 \\ 7.295 & 23.977 & 7.308 & -0.011 & 0.038 & -0.013 \\ 7.290 & 7.308 & 24.017 & 0.003 & 0.023 & 0.016 \\ 0.012 & -0.011 & 0.003 & 7.993 & -0.011 & 0.011 \\ 0.008 & 0.038 & 0.023 & -0.011 & 8.011 & 0.003 \\ -0.016 & -0.013 & 0.016 & 0.011 & 0.003 & 7.993 \end{bmatrix}, \text{GPa} \tag{14}$$

A comparison of this tensor with the one obtained using the direct description of different constituents reveals only minor discrepancies. The relative Frobenius error, computed as:

$$err = \frac{\left\| C_{VCCTL} - C_{VCCTL\_3PHASE} \right\|_F}{\left\| C_{VCCTL} \right\|_F} 100\%, \tag{15}$$

where $\|.\|_F$ denotes Frobenius norm, is 0.37% in this case. Therefore, we assumed that the results obtained from the model based on the microtomography data can be directly compared with those from the model based on the simulation of the hydration process. The effective elastic tensor determined on the basis of model from microtomographic data depicted in

10970207, 2025, 24, Downloaded from https://onlinelibrary.wiley.com/doi/10.1002/nme.70200 by Instytut Podstawowych Problemow Techniki PAN, Wiley Online Library on [11/12/2025]. See the Terms and Conditions (https://onlinelibrary.wiley.com/terms-and-conditions) on Wiley Online Library for rules of use; OA articles are governed by the applicable Creative Commons License

TABLE 4 | Effective elastic properties of cement paste using different microstructure models and Mori–Tanaka method, with errors provided relative to the CT-based model outcome, which is considered the reference solution.

Parameter	VCCTL-based (a = 300 μm)	VCCTL-based 3-phase model (a = 300 μm)	CT-based (a = 300 μm)	Mori–Tanaka (two-stage)	Mori–Tanaka (sequential)
Young modulus E, [GPa]	20.660 (2.81%)	20.567 (3.25%)	21.258 —	22.797 (7.24%)	21.655 (1.87%)
Shear modulus G, [GPa]	8.028 (4.48%)	7.999 (4.82%)	8.404 —	9.096 (8.24%)	8.673 (3.20%)
Poisson ratio ν	0.2330 (2.10%)	0.2334 (1.94%)	0.2380 —	0.2531 (6.35%)	0.2484 (4.37%)
Frobenius error ($\mathbf{C}_{CT}$ tensor taken as reference) *err*	4.46%	4.76%	—	12.05%	5.35%
Symmetry parameter s_r	0.0084	0.0097	0.0641	0	0
Symmetry parameter t_r	0.5997	0.5834	0.3451	0	0
Zener ratio a_r	0.9582	0.9594	0.9788	1	1

Figure 7 is presented below (size 300 μm):

$$C_{CT} = \begin{bmatrix} 24.502 & 7.765 & 7.784 & -0.160 & -0.038 & -0.051 \\ 7.765 & 25.207 & 7.840 & -0.229 & -0.115 & -0.019 \\ 7.784 & 7.841 & 25.197 & -0.086 & -0.112 & -0.090 \\ -0.160 & -0.229 & -0.086 & 8.364 & -0.020 & -0.050 \\ -0.038 & -0.115 & -0.112 & -0.020 & 8.469 & -0.095 \\ -0.051 & -0.019 & -0.090 & -0.050 & -0.095 & 8.379 \end{bmatrix}, \text{GPa} \tag{16}$$

A summary of the results obtained for the RVE with a size of 300 μm is presented in Table 4, where the provided effective elastic constants represent the averages of Young's modulus, Poisson's ratio, and shear modulus, calculated from values collected in different directions based on the effective elastic stiffness tensor. Moreover, results obtained by using the Mori–Tanaka method involving two-stage and sequential schemes are added. We have included the relative errors in brackets, taking the μCT-based model outcome as the reference solution. Besides the effective elastic properties we have included in the table the relative Frobenius error computed in a way presented in Equation (15), but utilizing as the reference the $\mathbf{C}_{CT}$ tensor. We have also included the symmetry parameters s_r and t_r as well as Zener ratio a_r. As previously mentioned, the results obtained from the model generated through the hydration process simulation (VCCTL) are in very good agreement with those obtained from the simplified three-phase model. The results obtained from the model built on microtomography data align well with the previously discussed VCCTL-based results. The Mori–Tanaka homogenization provides fair agreement with the numerical results, both two-stage and sequential approaches noticeably overestimate the effective shear modulus and Poisson ratio, but the two-stage approach leads to higher disparities. Although the Zener ratio is close to 1 for both the VCCTL-based and μCT-based models, a closer alignment with perfect isotropy is observed for the μCT-based model. The symmetry parameter t_r, which reflects the deviation from the best isotropic approximation, is also lower for the μCT-based model. However, the parameter s_r, which expresses the difference between the components of the stiffness tensor in the raw results (across different directions), is lower for the VCCTL-based model. In other words, while the CT-based model aligns better with the isotropic reference overall, the VCCTL-based model exhibits smaller directional discrepancies in its raw elastic constants.

3.2 | Influence of the RVE Size on the Effective Properties

Furthermore, the effective stiffness tensors have been determined for all cases of RVE sizes and spatial configurations described schematically in Figure 2. As shown in Figure 2, for each RVE size, eight different spatial configurations have been adopted. The effective elastic constants, determined from the stiffness tensors, are visualized in Figure 9 (the average of the values for different loading directions has been depicted). The resulting symmetry ratios s_r and t_r as well as the Zener ratio a_r are presented in Figure 10 (described by Equations (2), (5), and (10)) respectively.

10970207, 2025, 24, Downloaded from https://onlinelibrary.wiley.com/doi/10.1002/nme.70200 by Instytut Podstawowych Problemow Techniki PAN, Wiley Online Library on [11/12/2025]. See the Terms and Conditions (https://onlinelibrary.wiley.com/terms-and-conditions) on Wiley Online Library for rules of use; OA articles are governed by the applicable Creative Commons License

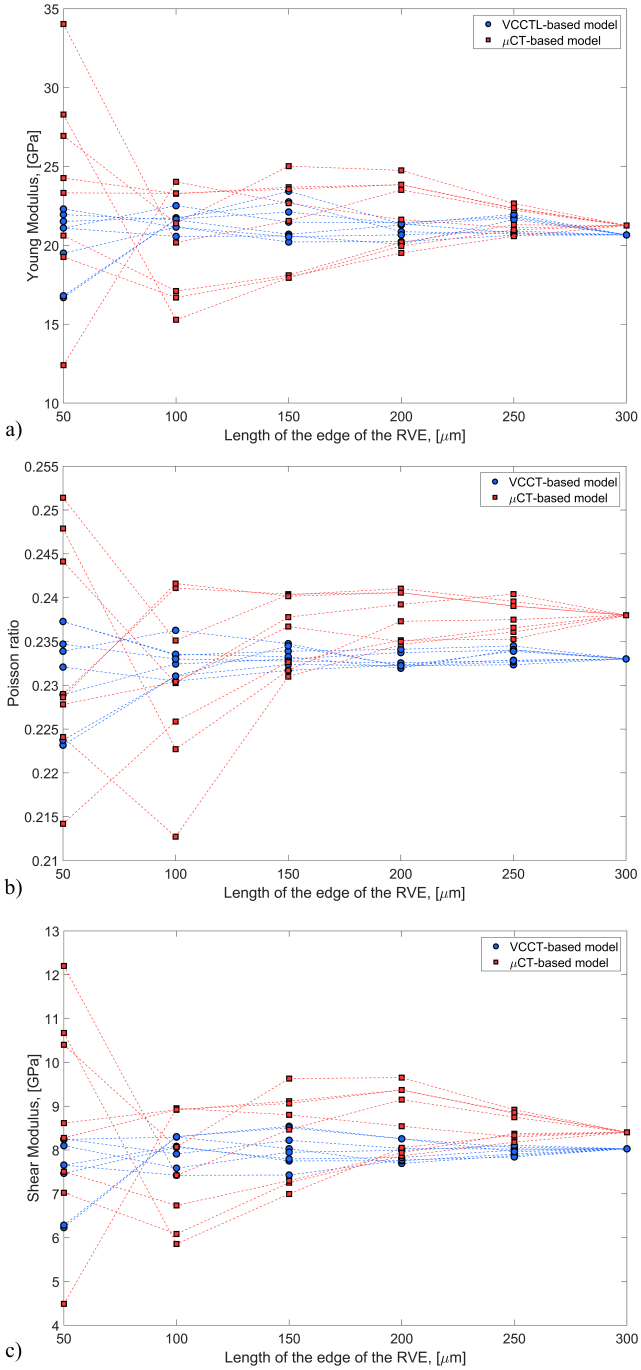

FIGURE 9 | Effective elastic constants (average of the values for different loading directions) in terms of the size and spatial configuration of the RVE (each curve presents results for different spatial configuration according to the scheme presented in Figure 2): (a) Young modulus, (b) Poisson ratio, (c) shear modulus.

The effective elastic constants obtained from the RVE analysis based on VCCTL software are less sensitive to RVE size than those derived from a model of the actual microstructure reconstructed from μCT data. This fact may be attributed to variations in the spatial distribution, shape characteristics, and size of clinker particles and pore agglomerates. In the case of VCCTL-based model, the results obtained with the RVE size 50 μm should be interpreted with caution since the effective elastic constants exhibit a relatively high degree of variability. Increasing the size to 100 μm significantly reduces this variability. However, for the μCT-based model, the variability of effective elastic constants for RVE sizes of 50 and 100 μm remains very high; μCT-based models of these sizes are therefore inadequate for determining the effective properties of cement paste. The presented results support the recommendation of Hlobil et al. [5], who stated that the RVE size for mechanical problems should be at least 150–200 μm to realistically represent cement grains. The

10970207, 2025, 24, Downloaded from https://onlinelibrary.wiley.com/doi/10.1002/nme.70200 by Instytut Podstawowych Problemow Techniki PAN, Wiley Online Library on [11/12/2025]. See the Terms and Conditions (https://onlinelibrary.wiley.com/terms-and-conditions) on Wiley Online Library for rules of use; OA articles are governed by the applicable Creative Commons License

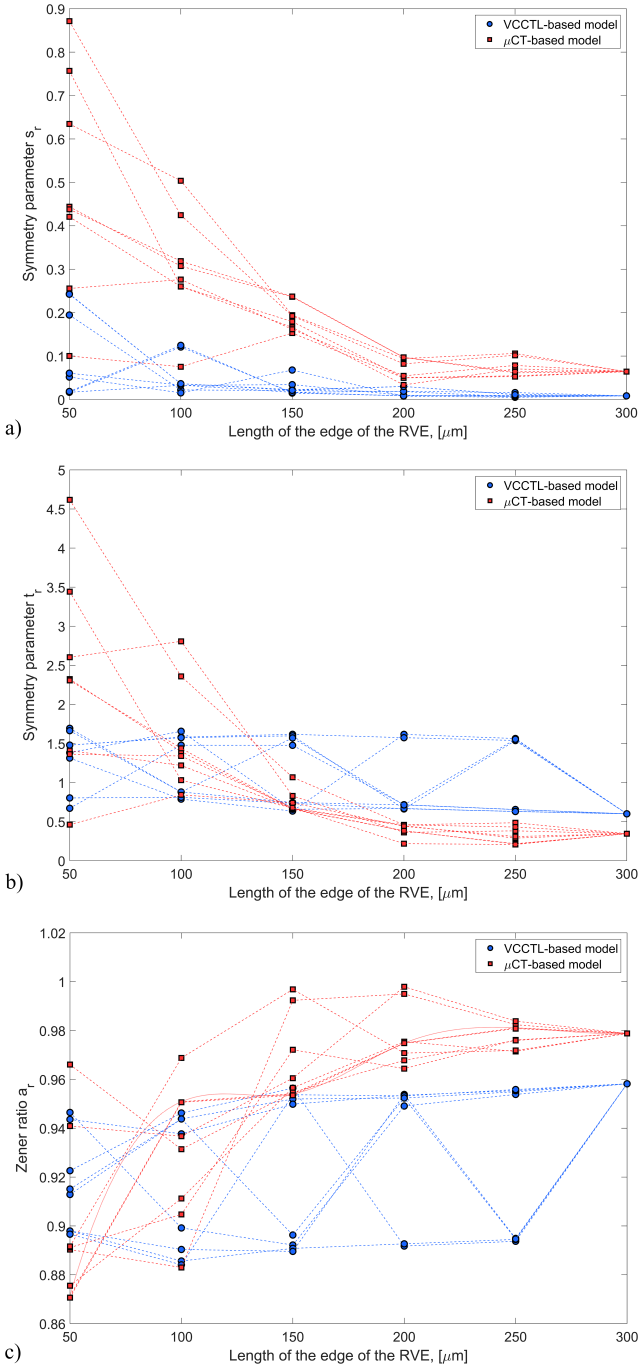

FIGURE 10 | Symmetry ratios in terms of of the size and spatial configuration of the RVE (each curve presents results for different spatial configuration according to the scheme presented in Figure 2): (a) s_r (Equation 2), (b) t_r (Equation 5), (c) a_r (Equation 10).

VCCTL-based model provides a more uniform distribution of cement paste constituents and a simplified shape within the RVE compared to the μCT-based model. On one hand, this enables good predictive capabilities for effective properties using smaller RVEs, but on the other hand, it distorts the view of local stiffness variability. Another significant distinction between results from various models lies in the symmetry properties of the stiffness tensor. Although the Zener ratio is below one for all analyzed cases, the symmetry of the stiffness tensor computed through the μCT-based model tends toward isotropy as the RVE size increases, but perfect isotropic symmetry is typically not achieved. In contrast, no relationship between the RVE size and the symmetry type of the stiffness tensor has been observed in the case of the VCCTL-based model. Regardless of the RVE size, the Zener ratio remains in the range of 0.88–0.96 (for the VCCTL-based model).

10970207, 2025, 24, Downloaded from https://onlinelibrary.wiley.com/doi/10.1002/nme.70200 by Instytut Podstawowych Problemow Techniki PAN, Wiley Online Library on [11/12/2025]. See the Terms and Conditions (https://onlinelibrary.wiley.com/terms-and-conditions) on Wiley Online Library for rules of use; OA articles are governed by the applicable Creative Commons License

3.3 | Stress Distribution at the Microscale Level

Besides the determination of the effective properties, we have also focused on the local distribution of stresses at the microscale level. We conducted numerical experiments of uniaxial compression involving $\varepsilon_{11} = -0.001$ for the model generated by simulating the hydration process and for the model incorporating microtomography data. RVE models of size $300 \times 300 \times 300\,\mu m$ are taken into account in the comparison. Figure 11 visualizes the distributions of the first principal stress, Figure 12 shows the distributions of the third principal stress while Figure 13 presents the distribution of the equivalent Huber–von Mises stress. In general, the stress ranges show fair agreement between the different models. However, the μCT-based solutions exhibit higher local stress concentrations, likely due to the more irregular shapes and distributions of anhydrous clinker grains and pores compared to the model based on hydration simulation. This statement is supported by results reported in works [62, 63], which show that, compared with spherical particles, nonspherical reinforcing particles in composites exhibit higher stress fluctuations. Furthermore, Figure 14 illustrates the probability

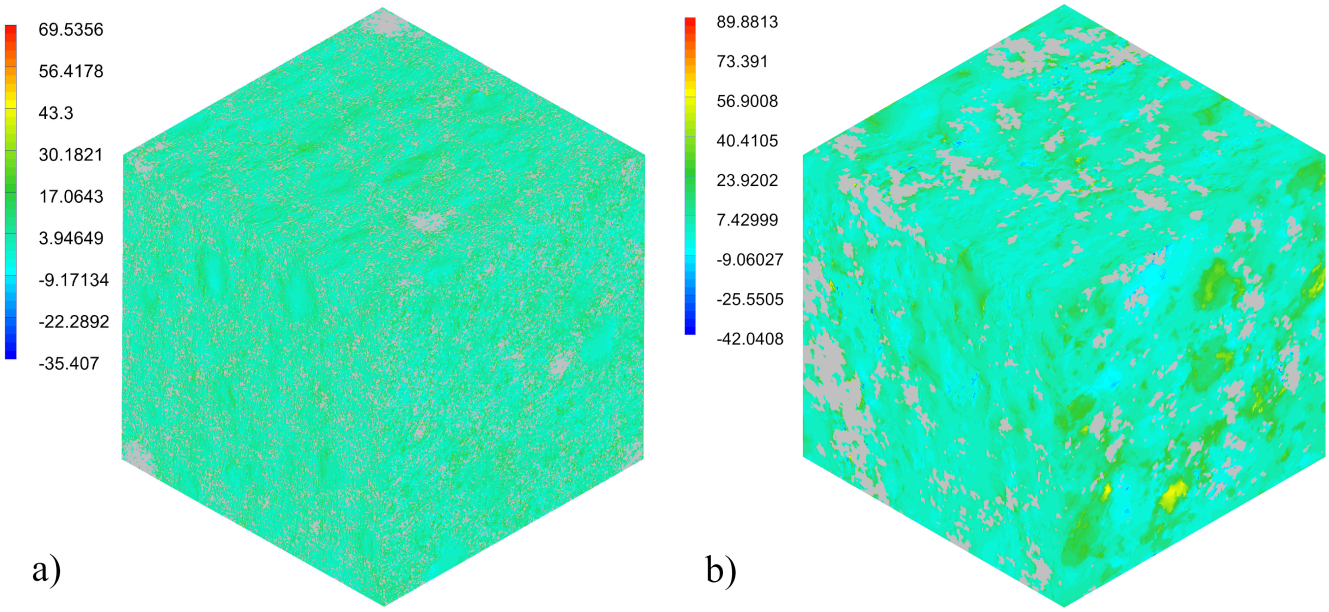

FIGURE 11 | Distribution of first principal stress: (a) VCCTL-based 3-phase model, (b) μCT-based model [MPa].

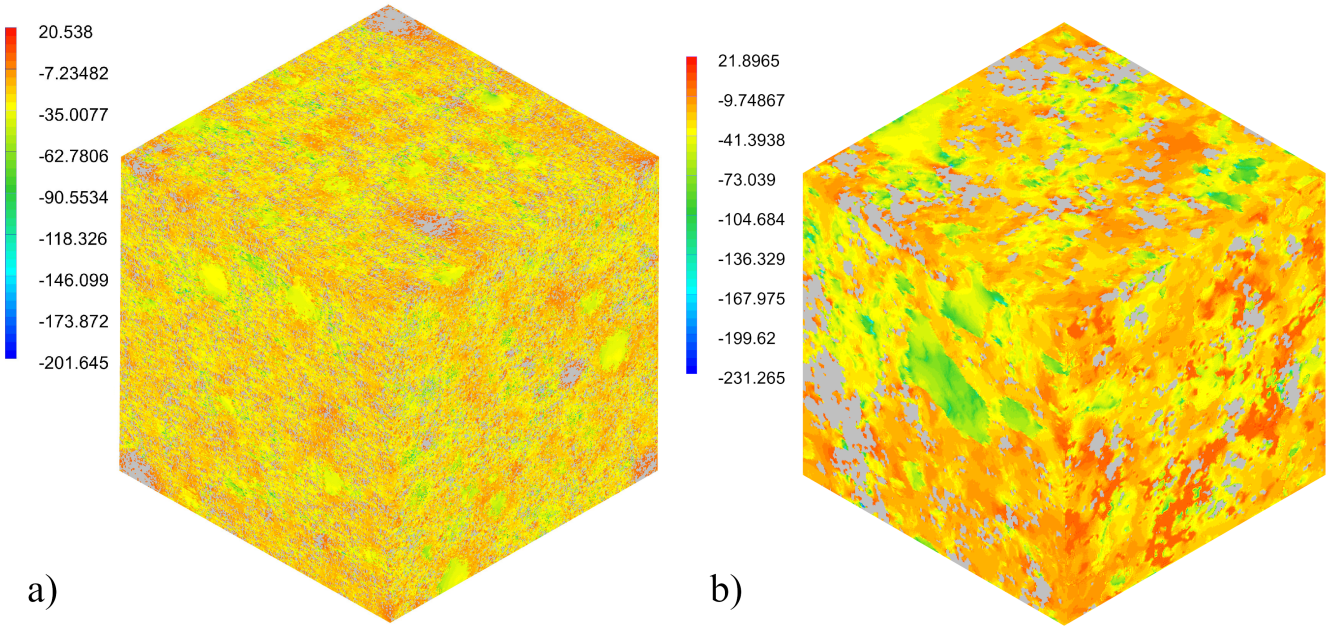

FIGURE 12 | Distribution of third principal stress: (a) VCCTL-based 3-phase model, (b) μCT-based model [MPa].

10970207, 2025, 24, Downloaded from https://onlinelibrary.wiley.com/doi/10.1002/nme.70200 by Instytut Podstawowych Problemow Techniki PAN, Wiley Online Library on [11/12/2025]. See the Terms and Conditions (https://onlinelibrary.wiley.com/terms-and-conditions) on Wiley Online Library for rules of use; OA articles are governed by the applicable Creative Commons License

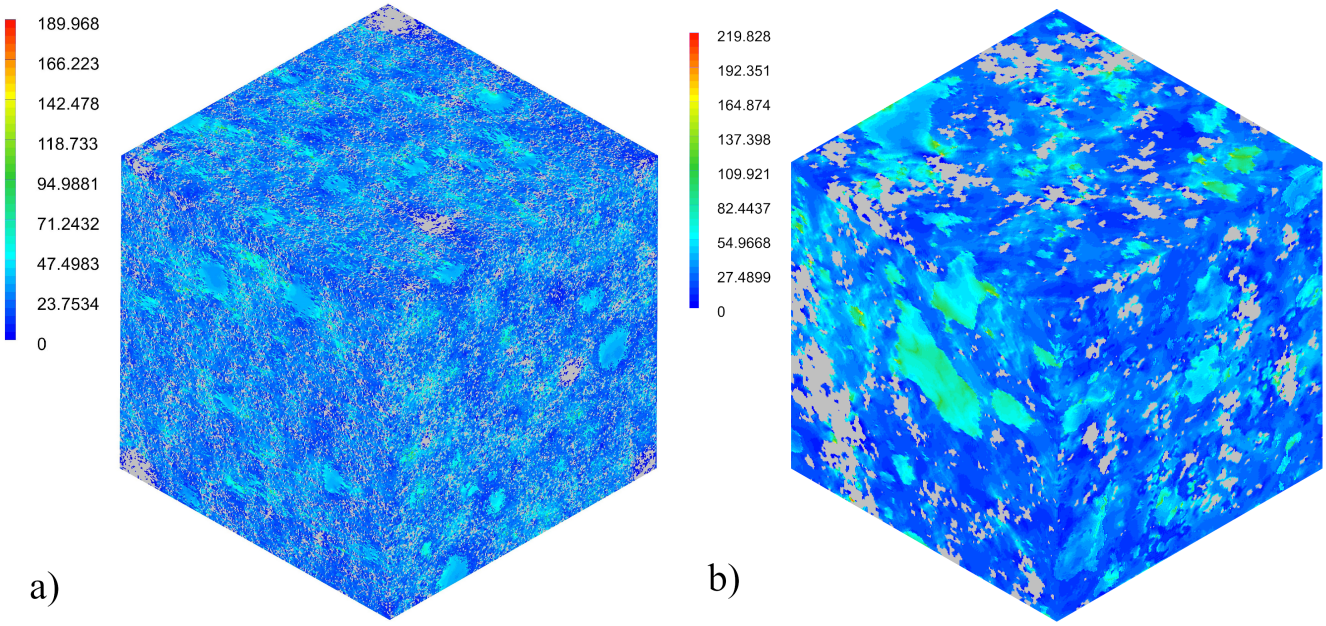

FIGURE 13 | Distribution of equivalent Huber-von Mises stress: (a) VCCTL-based 3-phase model, (b) μCT-based model [MPa].

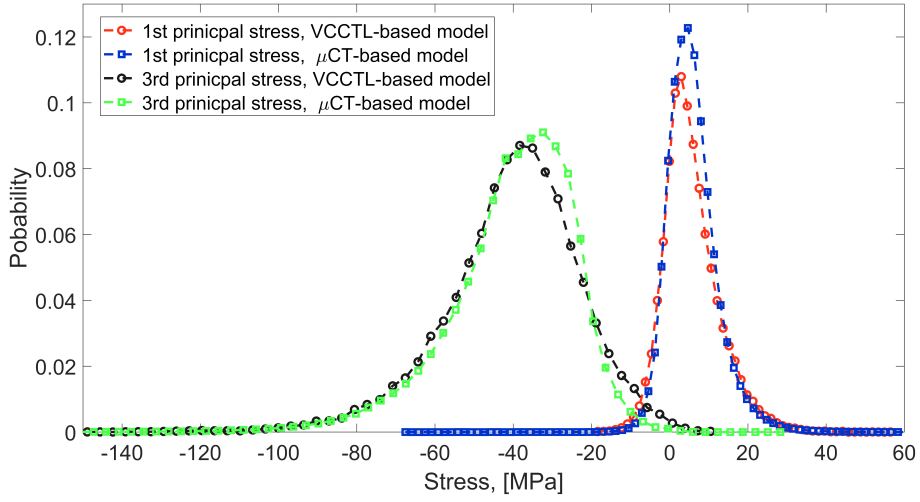

FIGURE 14 | Principal stress distributions (1st and 3rd principal stresses) in the anhydrous clinker grains obtained based on the models of the microstructure obtained from the VCCTL software and from the microtomographic data.

distribution of principal stress values in anhydrous clinker grains, computed based on results from both models. In this case, good agreement between the results obtained from both models can be observed.

4 | Conclusions

4.1 | General Remarks

In this paper, we conducted a detailed study on the elastic behavior of cement paste. By performing computational homogenization with different RVE sizes and using microstructure models generated from both hydration process simulations and microtomographic data, we arrived at the following conclusions:

– The effective elastic constants obtained from both microstructure models of size 300 μm are consistent. The relative errors between these results are 2.8% for Young's modulus, 4.5% for shear modulus, and 2.1% for Poisson's ratio.

10970207, 2025, 24, Downloaded from https://onlinelibrary.wiley.com/doi/10.1002/nme.70200 by Instytut Podstawowych Problemow Techniki PAN, Wiley Online Library on [11/12/2025]. See the Terms and Conditions (https://onlinelibrary.wiley.com/terms-and-conditions) on Wiley Online Library for rules of use; OA articles are governed by the applicable Creative Commons License

- The Mori–Tanaka method, when applied using a sequential scheme, aligns well with the results obtained from computational homogenization. The relative errors with respect to the μCT-based model are 1.9% for Young's modulus, 3.2% for the shear modulus, and 4.4% for Poisson's ratio. It is worth noting that this approach is highly time-efficient; however, a hydration simulation must be performed beforehand to determine the volume fractions of the phases.
- The effective elastic constants obtained from the μCT-based model, which represents the actual microstructure, are more sensitive to the RVE size than those derived from the VCCTL-based model. Consequently, a larger RVE size is required to determine effective properties when using the μCT-based model.
- Our findings support the recommendation in [5] that the RVE should be at least 150–200 μm to realistically represent cement grains in the case of the μCT-based model.
- The microstructure model generated from the hydration process exhibits good predictive capabilities for effective properties using smaller RVEs than the μCT-based model. However, it distorts the representation of local stiffness variability.
- Perfect isotropic symmetry of the stiffness tensor was not observed for all analyzed RVEs. However, the μCT-based model tends toward perfect isotropy as the RVE size increases. In contrast, no clear relationship between RVE size and stiffness tensor symmetry was observed for the VCCTL-based model.
- The stress distributions obtained for both models at a size of 300 μm are generally consistent. Although the μCT-based solutions exhibit higher local stress concentrations, the overall stress ranges show reasonable agreement between the two models.

4.2 | Limitations and Prospects

It is important to emphasize that a limitation of this study is the reliance on the elastic constants of the cement paste constituents taken from the literature. There is considerable variability in these values across different publications, so using another set of elastic constants for the phases may yield slightly different results. However, any potential differences in obtained effective elastic properties and stress distributions resulting from mentioned variations in the properties of constituents should not oppose the conclusions of this study. Another limitation of our study is the limited accuracy in representing the geometrical features of the microstructure, which is restricted by the resolutions available in the VCCTL software and μCT data. It should be emphasized that the presented results are based on computational models, and further investigation is necessary for experimental validation. Nonetheless, the study provides new insights into the variability of cement paste elastic properties in relation to different volume element sizes and types of microstructure models. The presented results may facilitate the preparation of RVE models by demonstrating that the required RVE size depends on the type of microstructure model and highlighting potential differences between results obtained for different RVE sizes.

Funding

The publication is supported by a grant implemented within the framework of the Excellence Initiative — Research University program, Silesian University of Technology (10/040/SDU/10-07-02) and partially by the Institute of Fundamental Technological Research of Polish Academy of Sciences.

Conflicts of Interest

The authors declare no conflicts of interest.

Data Availability Statement

The data that support the findings of this study are available from the corresponding author upon reasonable request.

References

1. H. Zhang, Y. Xu, Y. Gan, Z. Chang, E. Schlangen, and B. Šavija, "Microstructure Informed Micromechanical Modelling of Hydrated Cement Paste: Techniques and Challenges," *Construction and Building Materials* 251 (2020): 118983, https://doi.org/10.1016/j.conbuildmat.2020.118983.

2. D. P. Bentz, S. Mizell, S. Satterfield, et al., "The Visible Cement Data Set," *Journal of Research of the National Institute of Standards and Technology* 107 (2002): 137–148, https://doi.org/10.6028/jres.107.013.

10970207, 2025, 24, Downloaded from https://onlinelibrary.wiley.com/doi/10.1002/nme.70200 by Instytut Podstawowych Problemow Techniki PAN, Wiley Online Library on [11/12/2025]. See the Terms and Conditions (https://onlinelibrary.wiley.com/terms-and-conditions) on Wiley Online Library for rules of use; OA articles are governed by the applicable Creative Commons License

3. E. Gallucci, K. Scrivener, A. Groso, M. Stampanoni, and G. Margaritondo, "3D Experimental Investigation of the Microstructure of Cement Pastes Using Synchrotron X-Ray Microtomography (μCT)," *Cement and Concrete Research* 37 (2007): 360–368, https://doi.org/10.1016/j.cemconres.2006.10.012.

4. S. Y. Chung, J. S. Kim, D. Stephan, and T. S. Han, "Overview of the Use of Micro-Computed Tomography (Micro-CT) to Investigate the Relation Between the Material Characteristics and Properties of Cement-Based Materials," *Construction and Building Materials* 229 (2019): 116843, https://doi.org/10.1016/j.conbuildmat.2019.116843.

5. M. Hlobil, I. Kumpová, and A. Hlobilová, "Surface Area and Size Distribution of Cement Particles in Hydrating Paste as Indicators for the Conceptualization of a Cement Paste Representative Volume Element," *Cement and Concrete Composites* 134 (2022): 104798, https://doi.org/10.1016/j.cemconcomp.2022.104798.

6. M. Zhang and A. P. Jivkov, "Microstructure-Informed Modelling of Damage Evolution in Cement Paste," *Construction and Building Materials* 66 (2014): 731–742, https://doi.org/10.1016/j.conbuildmat.2014.06.017.

7. J. Huang, K. Krabbenhoft, and A. V. Lyamin, "Statistical Homogenization of Elastic Properties of Cement Paste Based on X-Ray Microtomography Images," *International Journal of Solids and Structures* 50 (2013): 699–709, https://doi.org/10.1016/j.ijsolstr.2012.10.030.

8. M. Zhang and A. P. Jivkov, "Micromechanical Modelling of Deformation and Fracture of Hydrating Cement Paste Using X-Ray Computed Tomography Characterisation," *Composites. Part B, Engineering* 88 (2016): 64–72, https://doi.org/10.1016/j.compositesb.2015.11.007.

9. J. S. Kim, J. H. Kim, and T. S. Han, "Microstructure Characterization of Cement Paste From Micro-CT and Correlations With Mechanical Properties Evaluated From Virtual and Real Experiments," *Materials Characterization* 155 (2019): 109807, https://doi.org/10.1016/j.matchar.2019.109807.

10. M. Hain and P. Wriggers, "Numerical Homogenization of Hardened Cement Paste," *Computational Mechanics* 42 (2008): 197–212, https://doi.org/10.1007/s00466-007-0211-9.

11. H. Zhang, B. Šavija, S. C. Figueiredo, M. Lukovic, and E. Schlangen, "Microscale Testing and Modelling of Cement Paste as Basis for Multi-Scale Modelling," *Materials (Basel)* 9 (2016): 907, https://doi.org/10.3390/ma9110907.

12. H. Zhang, B. Šavija, S. C. Figueiredo, and E. Schlangen, "Experimentally Validated Multi-Scale Modelling Scheme of Deformation and Fracture of Cement Paste," *Cement and Concrete Research* 102 (2017): 175–186, https://doi.org/10.1016/j.cemconres.2017.09.011.

13. H. Zhang, B. Šavija, and E. Schlangen, "Combined Experimental and Numerical Study on Micro-Cube Indentation Splitting Test of Cement Paste," *Engineering Fracture Mechanics* 199 (2018): 773–786, https://doi.org/10.1016/j.engfracmech.2018.04.018.

14. H. Zhang, B. Šavija, M. Luković, and E. Schlangen, "Experimentally Informed Micromechanical Modelling of Cement Paste: An Approach Coupling X-Ray Computed Tomography and Statistical Nanoindentation," *Composites. Part B, Engineering* 157 (2019): 109–122, https://doi.org/10.1016/j.compositesb.2018.08.102.

15. D. P. Bentz, "Three-Dimensional Computer Simulation of Cement Hydra- Tion and Microstructure Development," *Journal of the American Ceramic Society* 80, no. 1 (1997): 3–21.

16. D. P. Bentz, *CEMHYD3D: A Three-Dimensional Cement Hydration and Microstructure Development Modeling Package* (Interagency/Internal Report (NISTIR), National Institute of Standards and Technology, 2005).

17. K. van Breugel, "Numerical Simulation of Hydration and Microstructural Development in Hardening Cement-Based Materials (I) Theory," *Cement and Concrete Research* 25 (1995): 319–331, https://doi.org/10.1016/0008-8846(95)00017-8.

18. S. Bishnoi and K. L. Scrivener, "μic: A New Platform for Modelling the Hydration of Cements," *Cement and Concrete Research* 39 (2009): 266–274, https://doi.org/10.1016/j.cemconres.2008.12.002.

19. L. Valentini, M. Parisatto, V. Russo, et al., "Simulation of the Hydration Kinetics and Elastic Moduli of Cement Mortars by Microstructural Modelling," *Cement and Concrete Composites* 52 (2014): 54–63, https://doi.org/10.1016/j.cemconcomp.2014.05.005.

20. E. Garboczi, "Finite Element and Finite Difference Programs for Computing the Linear Electric and Elastic Properties of Digital Images of Random Materials," 1998 NIST Interagency/Internal Rep., 6269, 198.

21. D. A. Kulik, F. Winnefeld, A. Kulik, G. D. Miron, and B. Lothenbach, "CemGEMS—An Easy-To-Use Web Application for Thermodynamic Modelling of Cementitious Materials," *RILEM Technical Letters* 6 (2021): 36–52, https://doi.org/10.21809/rilemtechlett.2021.140.

22. Y. Zhou, W. Li, Y. Peng, et al., "Hydration and Fractal Analysis on Low-Heat Portland Cement Pastes Using Thermodynamics-Based Methods," *Fractal and Fractional* 7 (2023): 1–28, https://doi.org/10.3390/fractalfract7080606.

23. C. Haecker, E. J. Garboczi, J. W. Bullard, et al., "Modeling the Linear Elastic Properties of Portland Cement Paste," *Cement and Concrete Research* 35 (2005): 1948–1960.

24. H. Mazaheripour, R. Faria, G. Ye, E. Schlangen, J. Granja, and M. Azenha, "Microstructure-Based Prediction of the Elastic Behaviour of Hydrating Cement Pastes," *Applied Sciences* 8 (2018): 442, https://doi.org/10.3390/app8030442.

10970207, 2025, 24, Downloaded from https://onlinelibrary.wiley.com/doi/10.1002/nme.70200 by Instytut Podstawowych Problemow Techniki PAN, Wiley Online Library on [11/12/2025]. See the Terms and Conditions (https://onlinelibrary.wiley.com/terms-and-conditions) on Wiley Online Library for rules of use; OA articles are governed by the applicable Creative Commons License

25. A. Rhardane, F. Grondin, and S. Y. Alam, "Development of a Micro-Mechanical Model for the Determination of Damage Properties of Cement Pastes," *Construction and Building Materials* 261 (2020): 120514, https://doi.org/10.1016/j.conbuildmat.2020.120514.

26. V. Šmilauer and Z. P. Bažant, "Identification of Viscoelastic C-S-H Behavior in Mature Cement Paste by FFT-Based Homogenization Method," *Cement and Concrete Research* 40 (2010): 197–207, https://doi.org/10.1016/j.cemconres.2009.10.003.

27. H. Moulinec and P. Suquet, "A Fast Numerical Method for Computing the Linear and Nonlinear Mechanical Properties of Composites," *Comptes Rendus L'académie des Sci. Série II, Mécanique, Phys. Chim. Astron* 318 (1994): 1417–1423.

28. H. Moulinec and P. Suquet, "A Numerical Method for Computing the Overall Response of Nonlinear Composites With Complex Microstructure," *Computer Methods in Applied Mechanics and Engineering* 157 (1998): 69–94, https://doi.org/10.1016/S0045-7825(97)00218-1.

29. H. L. Nguyen and Q.D. To, "Conductivity of Composites With Multiple Polygonal Aggregates, Theoretical Estimates and Numerical Solutions From Polarization Series," *International Journal of Engineering Science* 123 (2018): 109–116, https://doi.org/10.1016/j.ijengsci.2017.11.005.

30. M. Magri, L. Adam, and J. Segurado, "Particle Size Effects in Ductile Composites: An FFT Homogenization Study," *Journal of the Mechanics and Physics of Solids* 160 (2022): 104759, https://doi.org/10.1016/j.jmps.2021.104759.

31. L. Taut and V. Monchiet, "Numerical Homogenization With FFT Method for Elastic Composites With Spring-Type Interfaces," *Composite Structures* 305 (2023): 116426, https://doi.org/10.1016/j.compstruct.2022.116426.

32. J. Vondřejc, J. Zeman, and I. Marek, "An FFT-Based Galerkin Method for Homogenization of Periodic Media," *Computers & Mathematics with Applications* 68 (2014): 156–173, https://doi.org/10.1016/j.camwa.2014.05.014.

33. M. Schneider, "A Review of Nonlinear FFT-Based Computational Homogenization Methods," *Acta Mechanica* 232 (2021): 2051–2100, https://doi.org/10.1007/s00707-021-02962-1.

34. C. Gierden, J. Kochmann, J. Waimann, B. Svendsen, and S. Reese, "A Review of FE-FFT-Based Two-Scale Methods for Computational Modeling of Microstructure Evolution and Macroscopic Material Behavior," *Archives of Computational Methods in Engineering* 29 (2022): 4115–4135, https://doi.org/10.1007/s11831-022-09735-6.

35. J. Escoda, F. Willot, D. Jeulin, J. Sanahuja, and C. Toulemonde, "Influence of the Multiscale Distribution of Particles on Elastic Properties of Concrete," *International Journal of Engineering Science* 98 (2016): 60–71, https://doi.org/10.1016/j.ijengsci.2015.07.010.

36. P. S. M. Thilakarathna, K. S. Kristombu Baduge, P. Mendis, H. Lee, E. R. K. Chandrathilaka, and V. Vimonsatit, "Multiscale Modelling Framework for Elasticity of Ultra High Strength Concrete Using Nano/Microscale Characterization and Finite Element Representative Volume Element Analysis," *Construction and Building Materials* 327 (2022): 126968, https://doi.org/10.1016/j.conbuildmat.2022.126968.

37. B. Bary, M. Ben Haha, E. Adam, and P. Montarnal, "Numerical and Analytical Effective Elastic Properties of Degraded Cement Pastes," *Cement and Concrete Research* 39 (2009): 902–912, https://doi.org/10.1016/j.cemconres.2009.06.012.

38. X. Gao, Y. Wei, and W. Huang, "Effect of Individual Phases on Multiscale Modeling Mechanical Properties of Hardened Cement Paste," *Construction and Building Materials* 153 (2017): 25–35, https://doi.org/10.1016/j.conbuildmat.2017.07.074.

39. C. Hu and Z. Li, "Micromechanical Investigation of Portland Cement Paste," *Construction and Building Materials* 71 (2014): 44–52, https://doi.org/10.1016/j.conbuildmat.2014.08.017.

40. B. Pichler, C. Hellmich, and J. Eberhardsteiner, "Spherical and Acicular Representation of Hydrates in a Micromechanical Model for Cement Paste: Prediction of Early-Age Elasticity and Strength," *Acta Mechanica* 203 (2009): 137–162, https://doi.org/10.1007/s00707-008-0007-9.

41. B. Pichler and C. Hellmich, "Upscaling Quasi-Brittle Strength of Cement Paste and Mortar: A Multi-Scale Engineering Mechanics Model," *Cement and Concrete Research* 41 (2011): 467–476, https://doi.org/10.1016/j.cemconres.2011.01.010.

42. Y. Li, Y. Liu, and R. Wang, "Evaluation of the Elastic Modulus of Concrete Based on Indentation Test and Multi-Scale Homogenization Method," *Journal of Building Engineering* 43 (2021): 102758, https://doi.org/10.1016/j.jobe.2021.102758.

43. M. Benzerzour, D. C. Chu, M. Amar, J. Kleib, and N. E. Abriak, "A Novel Approach Based on Microstructural Modeling and a Multi-Scale Model to Predicting the Mechanical-Elastic Properties of Cement Paste," *Case Studies in Construction Materials* 21 (2024): e03498, https://doi.org/10.1016/j.cscm.2024.e03498.

44. I. Pokorska, M. Poński, and T. Burczyński, "Multiscale Analysis of Cement Composites," *Computer Assisted Methods in Engineering and Science* 31 (2024): 507–518, https://doi.org/10.24423/cames.2024.1770.

45. M. Hlobil and I. Kumpová, "A Collection of Three-Dimensional Datasets of Hydrating Cement Paste," *Data in Brief* 46 (2023): 108903, https://doi.org/10.1016/j.dib.2023.108903.

46. S. Lucarini and J. Segurado, "On the Accuracy of Spectral Solvers for Micromechanics Based Fatigue Modeling," *Computational Mechanics* 63 (2019): 365–382, https://doi.org/10.1007/s00466-018-1598-1.

10970207, 2025, 24, Downloaded from https://onlinelibrary.wiley.com/doi/10.1002/nme.70200 by Instytut Podstawowych Problemow Techniki PAN, Wiley Online Library on [11/12/2025]. See the Terms and Conditions (https://onlinelibrary.wiley.com/terms-and-conditions) on Wiley Online Library for rules of use; OA articles are governed by the applicable Creative Commons License

47. G. Constantinides and F. J. Ulm, "The Effect of Two Types of C-S-H on the Elasticity of Cement-Based Materials: Results From Nanoindentation and Micromechanical Modeling," *Cement and Concrete Research* 34 (2004): 67–80, https://doi.org/10.1016/S0008-8846(03)00230-8.

48. K. Velez, S. Maximilien, D. Damidot, G. Fantozzi, and F. Sorrentino, "Determination by Nanoindentation of Elastic Modulus and Hardness of Pure Constituents of Portland Cement Clinker," *Cement and Concrete Research* 31 (2001): 555–561, https://doi.org/10.1016/S0008-8846(00)00505-6.

49. S. Hajilar and B. Shafei, "Nano-Scale Investigation of Elastic Properties of Hydrated Cement Paste Constituents Using Molecular Dynamics Simulations," *Computational Materials Science* 101 (2015): 216–226, https://doi.org/10.1016/j.commatsci.2014.12.006.

50. "Digimat User Manual," Release 2021.2, MSC Software Belgium SA, 2021.

51. M. El Fallaki Idrissi, F. Praud, V. Champaney, F. Chinesta, and F. Meraghni, "Multiparametric Modeling of Composite Materials Based on Non-Intrusive PGD Informed by Multiscale Analyses: Application for Real-Time Stiffness Prediction of Woven Composites," *Composite Structures* 302 (2022): 116228, https://doi.org/10.1016/j.compstruct.2022.116228.

52. F. Cavallini, "The Best Isotropic Approximation of an Anisotropic Hooke's Law," *Bollettino di Geofisica Teorica ed Applicata* 40 (1999): 1–18.

53. Z. Li and R. C. Bradt, "The Single-Crystal Elastic Constants of Cubic (3C) SiC to 1000°C," *Journal of Materials Science* 22 (1987): 2557–2559, https://doi.org/10.1007/BF01082145.

54. M. Mele, G. Milan, A. Paffetti, et al., "Homogenization and Artificial Neural Network Prediction of Elastic Properties in Triply Periodic Minimal Surface Structures," *Progress in Additive Manufacturing* 10 (2025): 9337–9353, https://doi.org/10.1007/s40964-025-01165-7.

55. J. Fu, P. Sun, Y. Du, H. Li, X. Zhou, and Q. Tian, "Isotropic Design and Mechanical Characterization of TPMS-Based Hollow Cellular Structures," *Composite Structures* 279 (2022): 114818, https://doi.org/10.1016/j.compstruct.2021.114818.

56. C. Naili, I. Doghri, and J. Demey, "Porous Materials Reinforced With Short Fibers: Unbiased Full-Field Assessment of Several Homogenization Strategies in Elasticity," *Mechanics of Advanced Materials and Structures* 29 (2022): 2857–2872, https://doi.org/10.1080/15376494.2021.1880674.

57. Y. Benveniste, "A New Approach to the Application of Mori-Tanaka's Theory in Composite Materials," *Mechanics of Materials* 6 (1987): 147–157, https://doi.org/10.1016/0167-6636(87)90005-6.

58. T. Mura, *Micromechanics of Defects in Solids* (Martinus Nijhoff Publishers, 1987).

59. Y. Koutsawa, G. Rauchs, D. Fiorelli, A. Makradi, and S. Belouettar, "A Multi-Scale Model for the Effective Electro-Mechanical Properties of Short Fiber Reinforced Additively Manufactured Ceramic Matrix Composites Containing Carbon Nanotubes," *Composites Part C: Open Access* 7 (2022): 100234, https://doi.org/10.1016/j.jcomc.2022.100234.

60. N. Otsu, "A Threshold Selection Method From Gray-Level Histograms," *IEEE Transactions on Systems, Man, and Cybernetics* 9 (1979): 62–66.

61. Y. S. Wang and J. G. Dai, "X-Ray Computed Tomography for Pore-Related Characterization and Simulation of Cement Mortar Matrix," *NDT and E International* 86 (2017): 28–35, https://doi.org/10.1016/j.ndteint.2016.11.005.

62. C. R. Chen, C. R. Qin, S. X. Li, and J. L. Wen, "Finite Element Analysis About Effects of Particle Morphology on Mechanical Response of Composites," *Materials Science & Engineering, A: Structural Materials: Properties, Microstructure and Processing* 278 (2000): 96–105, https://doi.org/10.1016/s0921-5093(99)00603-6.

63. A. Rasool and H. J. Böhm, "Effects of Particle Shape on the Macroscopic and Microscopic Linear Behaviors of Particle Reinforced Composites," *International Journal of Engineering Science* 58 (2012): 21–34, https://doi.org/10.1016/j.ijengsci.2012.03.022.

10970207, 2025, 24, Downloaded from https://onlinelibrary.wiley.com/doi/10.1002/nme.70200 by Instytut Podstawowych Problemow Techniki PAN, Wiley Online Library on [11/12/2025]. See the Terms and Conditions (https://onlinelibrary.wiley.com/terms-and-conditions) on Wiley Online Library for rules of use; OA articles are governed by the applicable Creative Commons License

Appendix A

List of Symbols and Their Descriptions

Table A1 provides a list of the symbols used in the paper along with their description.

TABLE A1 | List of symbols and their descriptions.

Symbol	Description
a	Length of the edge of cube associated with the RVE
a_r	Zener ratio (Equation 10)
$\mathbf{A}$	Strain concentration tensor
$\mathbf{C}_p$	Elastic stiffness tensor associated with phase p
$\mathbf{C}_{MT}$	Elastic stiffness tensor determined using Mori–Tanaka method
$\mathbf{C}_m$	Elastic stiffness tensor for matrix material
$\mathbf{C}_i$	Elastic stiffness tensor for inhomogeneity material
$\mathbf{C}_{CT}$	Elastic stiffness tensor determined through FFT-based homogenization utilizing microtomographic-based model
$\mathbf{C}_{VCCTL}$	Elastic stiffness tensor determined through FFT-based homogenization utilizing the outcome of hydration based model
$\mathbf{C}_{VCCTL\_3PHASE}$	Elastic stiffness tensor determined through FFT-based homogenization utilizing the simplified 3 phase model
$\mathbf{C}^{ISO}$	Elastic stiffness tensor approximated by the method of best isotropic approximation of an anisotropic tensor
$\tilde{C}_{ij}$	Average value of stiffness tensor component computed by averaging as presented by Equation (4)
$\mathbf{E}$	Prescribed macroscopic strain tensor
E	Young modulus
E_H	Effective Young modulus for hydration products
E_{AN}	Effective Young modulus for anhydrous clinker
err	Relative Frobenius error
f_m	Volume fraction of matrix
f_i	Volume fraction of inhomogeneity
G	Shear modulus
$\mathbf{I}$	Identity tensor
$\mathbf{R}$	Matrix used for calculation of symmetry parameter s_r
s_r	Symmetry parameter described by Equation (2)
$\mathbf{S}$	Eshelby's tensor
t_r	Symmetry parameter described by Equation (5)
$\mathbf{u}$	Displacement vector
$\mathbf{Z}$	Matrix used for calculation of symmetry parameter t_r
$\boldsymbol{\varepsilon}$	Strain tensor
ν	Poisson ratio
ν_H	Effective Poisson ratio for hydration products
ν_{AN}	Effective Poisson ratio for anhydrous clinker
λ, μ	Lame constants approximated by the method of best isotropic approximation of an anisotropic tensor (Equations (8) and (9))
$\boldsymbol{\sigma}$	Stress tensor
Ω	Volume domain of the RVE

10970207, 2025, 24, Downloaded from https://onlinelibrary.wiley.com/doi/10.1002/nme.70200 by Instytut Podstawowych Problemow Techniki PAN, Wiley Online Library on [11/12/2025]. See the Terms and Conditions (https://onlinelibrary.wiley.com/terms-and-conditions) on Wiley Online Library for rules of use; OA articles are governed by the applicable Creative Commons License

Appendix B

Differences Between Two Independently Generated Microstructure Models Using the Hydration Process Simulation

In this appendix, we present results for an additional microstructure model generated by simulating the hydration process. The objective is to quantify the relative differences between two independently generated models using the VCCTL software. Table B1 reports the phase volume fractions from two independent hydration simulations: the model used in the main text (Figure 1) and the additional model shown in Figure B1. The additional model has the same dimensions as the model in Figure 1 ($300 \times 300 \times 300\ \mu m$). The predicted phase volume fractions are very close, particularly for the phases with the greatest volume fractions. We also performed homogenization for the additional model. The resulting effective stiffness tensor is given in Equation (B1). Table B2 compares the effective elastic constants as well as the symmetry parameters for the two models (in the similar fashion as Table 4 in the main text). The relative differences in the elastic constants are below 1%. We therefore conclude that two independently generated microstructure models obtained from hydration simulations lead to very close stiffness predictions.

$$C_{VCCTL\_B} = \begin{bmatrix} 24.269 & 7.362 & 7.377 & 0.009 & 0.011 & -0.016 \\ 7.362 & 24.222 & 7.389 & 0.005 & 0.007 & -0.002 \\ 7.377 & 7.389 & 24.279 & -0.004 & 0.002 & -0.010 \\ 0.009 & 0.005 & -0.004 & 8.067 & -0.005 & 0.016 \\ 0.011 & 0.007 & 0.002 & -0.005 & 8.097 & -0.004 \\ -0.016 & -0.002 & -0.010 & 0.016 & -0.004 & 8.089 \end{bmatrix}, \text{GPa} \tag{B1}$$

TABLE B1 | Volume fractions for the microstructure models generated through independent simulations of the hydration process, relative errors with respect to the volume fraction 1 presented in brackets.

Phase	Volume fraction 1 (model used in the paper depicted in Figure 1)	Volume fraction 2 (additional model for verification depicted in Figure B1)
C-S-H (calcium silicate hydrate)	0.4392	0.4397 (0.11%)
CH (portlandite)	0.1750	0.1745 (0.29%)
Porosity	0.1678	0.1662 (0.95%)
C_3S (alite)	0.0709	0.0706 (0.42%)
C_2S (belite)	0.0081	0.0079 (2.47%)
C_3A (cubic tricalcium aluminate)	0.0046	0.0047 (2.17%)
C_4AF (tetracalcium aluminoferrite)	0.0261	0.0269 (3.07%)
Ettringite	0.0563	0.0563 (0.00%)
AFm (generic monosulfate)	0.0186	0.0187 (0.54%)
C_3AH_6 (hydrogarnet)	0.0333	0.0345 (3.60%)

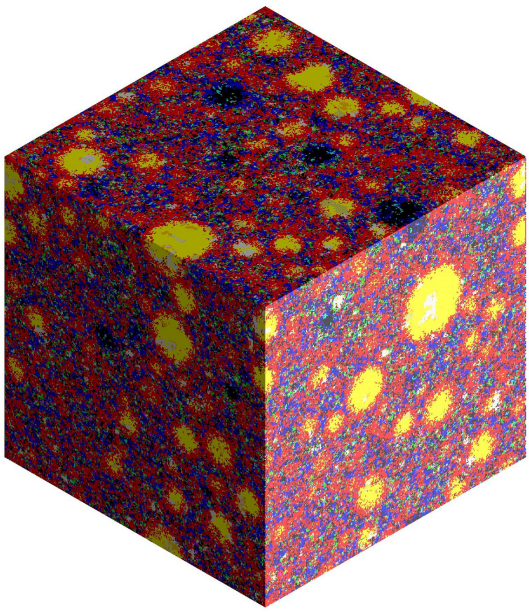

FIGURE B1 | Virtual model of the cement paste microstructure generated as the outcome of the hydration simulation, additional model for verification.

10970207, 2025, 24, Downloaded from https://onlinelibrary.wiley.com/doi/10.1002/nme.70200 by Instytut Podstawowych Problemow Techniki PAN, Wiley Online Library on [11/12/2025]. See the Terms and Conditions (https://onlinelibrary.wiley.com/terms-and-conditions) on Wiley Online Library for rules of use; OA articles are governed by the applicable Creative Commons License

TABLE B2 | Effective elastic properties and symmetry parameters of cement paste from two independent VCCTL-based models; relative errors with respect to the main-text model are given in brackets.

Parameter	VCCTL-based (model used in the paper depicted in Figure 1) (a = 300 μm)	VCCTL-based (additional model for verification depicted in Figure B1) (a = 300 μm)
Young modulus E, [GPa]	20.660 —	20.817 (0.76%) —
Shear modulus G, [GPa]	8.028 —	8.084 (0.71%)
Poisson ratio ν	0.2330 —	0.2332 (0.07%)
Frobenius error (VCCTL-based result taken as reference) *err*	—	0.82%
Symmetry parameter s_r	0.0084	0.0109
Symmetry parameter t_r	0.5997	0.6045
Zener ratio a_r	0.9582	0.9578

10970207, 2025, 24, Downloaded from https://onlinelibrary.wiley.com/doi/10.1002/nme.70200 by Instytut Podstawowych Problemow Techniki PAN, Wiley Online Library on [11/12/2025]. See the Terms and Conditions (https://onlinelibrary.wiley.com/terms-and-conditions) on Wiley Online Library for rules of use; OA articles are governed by the applicable Creative Commons License